nature communications

Article

https://doi.org/10.1038/s41467-025-57573-4

Sulfur-doping tunes *p-d* orbital coupling over asymmetric Zn-Sn dual-atom for boosting CO_2 electroreduction to formate

Received: 29 February 2024

Accepted: 26 February 2025

Published online: 05 March 2025

Check for updates

Bo Peng[1,2], Hao She[3], Zihao Wei[1], Zhiyi Sun[1], Ziwei Deng[1], Zhongti Sun[3] & Wenxing Chen[1]

The interaction of *p-d* orbitals at bimetallic sites plays a crucial role in determining the catalytic reactivity, which facilitates the modulation of charges and enhances the efficiency of CO_2 electroreduction process. Here, we show a ligand co-etching approach to create asymmetric Zn-Sn dual-atom sites (DASs) within metal-organic framework (MOF)-derived yolk-shell carbon frameworks (named Zn_1Sn_1/SNC). The DASs comprise one Sn center (*p*-block) partially doped with sulfur and one Zn center (*d*-block) with N coordination, facilitating the coupling of *p-d* orbitals between the Zn-Sn dimer. The N-Zn-Sn-S/N arrangement displays an asymmetric distribution of charges and atoms, leading to a stable adsorption configuration of HCOO* intermediates. In H-type cell, Zn_1Sn_1/SNC exhibits an impressive formate Faraday efficiency of 94.6% at -0.84 V. In flow cell, the asymmetric electronic architecture of Zn_1Sn_1/SNC facilitates high accessibility, leading to a high current density of -315.2 mA cm^{-2} at -0.90 V. Theoretical calculations show the asymmetric sites in Zn_1Sn_1/SNC with ideal adsorption affinity lower the CO_2 reduction barrier, thus improve the overall efficiency of CO_2 reduction.

The overabundance of greenhouse gases in the atmosphere is currently leading to a multitude of environmental issues[1–4]. There is an urgent need to expeditiously advance the development of effective and sustainable technologies aimed at converting CO_2 into valuable chemicals, in order to facilitate the process of carbon recycling[5–10]. The electroreduction reaction of CO_2 (CO_2RR) offers a sustainable solution for achieving the goal[11–14]. However, the significant variation in product distribution increases the economic cost of the product separation process[15–19]. Formate serves as a significant medium for the storage of hydrogen, allowing for the safe and effective containment of hydrogen energy in a liquid state, thereby ensuring the safety of hydrogen storage and transportation[20–23]. Specifically, the conversion of CO_2 to formate involves a two-electron transfer mechanism, with an initial potential of −0.19 V vs. RHE[24]. The conversion of CO_2 to formate exhibits a lower overpotential in comparison to the multi-electron transfer processes involved in reducing CO_2 to C_{2+} compounds[25–29]. However, the current overpotential and selectivity remain inadequate. Consequently, the development of effective catalysts to minimize energy consumption and enhance the selectivity for formic acid production is of paramount importance.

Recently, the Sn-based materials show great potential for CO_2-to-formate. According to reports, the Sn single-site catalysts, characterized by a well-defined local structure, have the ability to selectively convert CO_2 into formate or CO[30–33]. Catalysts with atomically dispersed interacting binuclear metal sites demonstrate greater intrinsic activity compared to single-site in complex catalytic environments, such as CO_2RR[28,34,35]. The interaction between the binuclear sites has the potential to enhance the affinity of the intermediates in the

[1]Energy & Catalysis Center, School of Materials Science & Engineering, Beijing Institute of Technology, Beijing 100081, China. [2]Guangxi Key Laboratory of Polysaccharide Materials and Modification, Laboratory of Chemical and Biological Trans-forming Process of Guangxi Higher Education Institutes, School of Chemistry and Chemical Engineering, Guangxi Minzu University, Nanning 530008, China. [3]School of Materials Science and Engineering, Jiangsu University, Zhen-Jiang, Jiangsu 212013, PR China. e-mail: wxchen@bit.edu.cn

catalytic process[36–38]. The current binuclear metal sites can be customized and effectively produced by the fine regulation of local active structure. Furthermore, there is a unique orbital coupling effect between different groups of metals. The coupling of *p-d* orbitals leads to the creation of hybridized orbitals, typically characterized by elevated energy levels in comparison to the original orbitals. the hybridized orbitals are able to effectively engage in the creation or breaking of coordination bonds in dynamic process, thereby improving the reactivity of the system. Furthermore, *p-d* orbital coupling can facilitate enhanced orbital overlap, thereby increasing the likelihood of coordination bond formation[39–41]. This slight modification in the distribution of electrons within the orbitals results in a fundamental shift in the bonding potential between the metallic elements, consequently influencing the catalytic properties in a synergistic manner[42–45]. Simultaneously, the presence of dual-atom sites (DASs) can result in a notably uneven distribution of charge polarization. However, it is difficult to precisely tune the DASs in order to enhance the *p-d* coupling effect and thus improve catalytic properties; such regulation also remains a significant challenge.

Herein, an asymmetric Zn-Sn dimer with partial sulfur doping, dispersed atomically on carbon frameworks in a yolk-shell configuration, demonstrates significant catalytic activity for the CO_2RR through a ligand coetching protocol (denoted as Zn_1Sn_1/SNC). The local structural modulation of the metal dual-sites and the constucted yolk-shell structure not only promotes the coupling of Zn-Sn centers but also presents high catalytic accessibility. The Zn_1Sn_1/SNC demonstrated a notable formate Faraday efficiency ($FE_{formate}$) of 94.6% at −0.84 V in the H-cell, and achieved current densities of up to −315.2 mA cm^{-2} at −0.90 V when integrated into the gas diffusion electrode of the flow cell. Density functional theory (DFT) calculations indicate that the introduction of partial S doping into Zn-Sn DASs disrupts the local symmetry, resulting in a gradual reduction in the number of electrons transferred to the Sn center. This leads to a significant enhancement in the electron storage capacity of Zn_1Sn_1/SNC. As a result, the reduction of the energy barrier can enhance the efficiency of the transformation of CO_2-to-formate.

Results and discussion

Synthesis and structural characterizations of Zn_1Sn_1/SNC

The Zn_1Sn_1/SNC was synthesized via one-step ligand co-etching method, depicted in Fig. 1a. Initially, a typical bimetallic ZnSn-MOFs polyhedron, was formed by merging Zn and Sn metal nodes with 2-methylimidazole as a coordinating ligand in a methanol solution (Supplementary Fig. 1). The MOF structure serves as a robust macrostructure for the subsequent carburization process. Subsequently, a blend of sulfur powder and dicyandiamide was added to introduce specific coordinating elements for structural adjustment. The pyrolysis process included swift heating to 1000 °C in Ar atmosphere, followed for 2 h, disrupting the ordered MOF structure[46]. The combination of gaseous S-ligands and corrosive ammonia generated by dicyandiamide collaboratively corrodes the primary framework of MOF[47]. This process results in the creation of a highly permeable yolk-shell main structure and the formation of partially sulfur-coordinated asymmetric Zn-Sn diatomic sites. Moreover, by maintaining an optimal carburization temperature, certain Zn nodes evaporated and transformed into individual atoms, while the Sn atoms remained dispersed at the atomic level. The mass composition of Zn and Sn was determined to be 0.41 wt% and 0.39 wt%, respectively, using inductively coupled plasma optical emission spectroscopy analysis (Table S1).

The ZIF-8 material is characterized by its abundant molecular cages that exhibit a strong spatial confinement effect, making it a highly suitable template for the encapsulation of metal species. Pyrolysis treatment yields carbon materials with numerous ligands, abundant defects, and high specific surface areas. Additionally, the unique spatial structure provided by MOF materials modifies the coordination environment of metal atoms and increases spatial separation between metal sites. In the pyrolysis process, the majority of Zn atoms undergo evaporation, leading to the dispersion of Zn atoms which have a tendency to bond with Sn atoms, forming the Zn-Sn dual sites. The formation of these atomic pairs may cause changes in electronic configurations or bonding types because of variations in the intrinsic reactivity of metal types. As such, the Sn content should not be excessively high to guarantee the controlled formation of atomic pairs without aggregation.

The scanning electron microscope (SEM) shows that Zn_1Sn_1/SNC has a unique polyhedron structure (Fig. 1b and Supplementary Note 1). Transmission electron microscopy (TEM) images and scanning TEM (STEM) exhibit that the Zn_1Sn_1/SNC has a well-defined yolk-shell architecture formed by a textured outer shell and a dense inner core. The same is true for comparison Sn_1/SNC sample (Fig. S3), showing a similar yolk-shell structure. Different structures are observed in the corresponding Sn_1/NC, and Zn_1/NC catalysts due to variations in preparation methods (Figs. S4–S5). This suggests that the combined use of cyanamide and sulfur powder during synthesis is crucial for effectively modulating ZIF-8. The N_2 adsorption-desorption isotherms show that the modified polyhedron structure of Zn_1Sn_1/SNC has a large surface area of 1582.3 $m^2 g^{-1}$, illustrating good accessibility for reactive species and efficient mass transfer (Supplementary Fig. 6). The energy dispersive X-ray spectroscopy (EDS, Fig. 1d) shows a homogeneous dispersion of Zn, Sn, and light elements S, C, and N. Such distributions also confirm the global morphology composition of Zn_1Sn_1/SNC. The distribution of metals over Zn_1Sn_1/SNC was examined using aberration-corrected STEM (AC-STEM), as illustrated in Fig. 1e, f. The results indicate the absence of distinct particles in Zn_1Sn_1/SNC, suggesting atomic-level dispersion of Zn-Sn atomic pairs. Atomically dispersed species are highlighted by red ellipses, representing Zn-Sn atomic pairs. Likewise, metal species in Sn_1/SNC, Sn_1/NC, and Zn_1/NC samples are distributed atomically (Supplementary Figs. S7–8). Zn-Sn atomic pairs are visualized using three-dimensional (3D) resolution images (Fig. 1g), which the positions of Zn-Sn atomic pairs show prominent color peaks. Statistical analysis is performed on the types and distances of metal pairs in Fig. 1f. Zn and Sn atoms do not exclusively form diatomic pairs; instead, some form single sites. Zn-Sn atomic pairs constitute 66.3% of the total composition (Fig. 1h). The average distance between Zn-Sn pairs is about 2.5 Å, closely matching the expected bond length for direct Zn-Sn coordination according to theoretical considerations.

Only two carbon signature peaks are appeared on the Zn_1Sn_1/SNC, Sn_1/SNC, Sn_1/NC, and Zn_1/NC catalysts, as evidenced by X-ray diffraction (XRD) measurement (Supplementary Fig. 9). No metal peaks corresponding to Zn or Sn are detected in the four samples, suggesting the lack of visible nanoparticles. X-ray photoelectron spectroscopy (XPS) is used to analyze the chemical states and elemental types of C, N, and S in Zn_1Sn_1/SNC. As shown in Supplementary Fig. 10a, the C−S bond peak (284.2 eV) in the C *1s* spectrum confirms the successful introduction of S into the carbon framework. The N *1 s* spectrum (Supplementary Fig. 10b) shows four main types of nitrogen species in Zn_1Sn_1/SNC: pyridinic N (398.3 eV), Zn/Sn-N_x (399.8 eV), pyrrolic N (401.2 eV), and graphitic N (403.9 eV). These results indicate the existence of M-N_x coordination in Zn_1Sn_1/SNC[48]. The fitting results of the S *2p* spectrum display characteristic peaks related to the thiophene-like C-S-C structure (S $2p_{3/2}$, $2p_{1/2}$) and oxidized S, confirming the incorporation of S into the nitrogen-doped carbon framework. The coordination structure of light elements in Zn_1Sn_1/SNC can be thoroughly examined using synchrotron-radiation soft X-ray absorption spectroscopy (Fig. 2a, b and Supplementary Note. 2)[49,50]. The C K-edge spectrum mainly consists of three distinct peaks attributed to π*C=C transition, π*C-N, and σ*C-C transition. The alignment of these chemical bonds arises from the movement of electrons to antibonding orbitals through dipole transitions. As for the N spectrum, it exhibits

https://doi.org/10.1038/s41467-025-57573-4

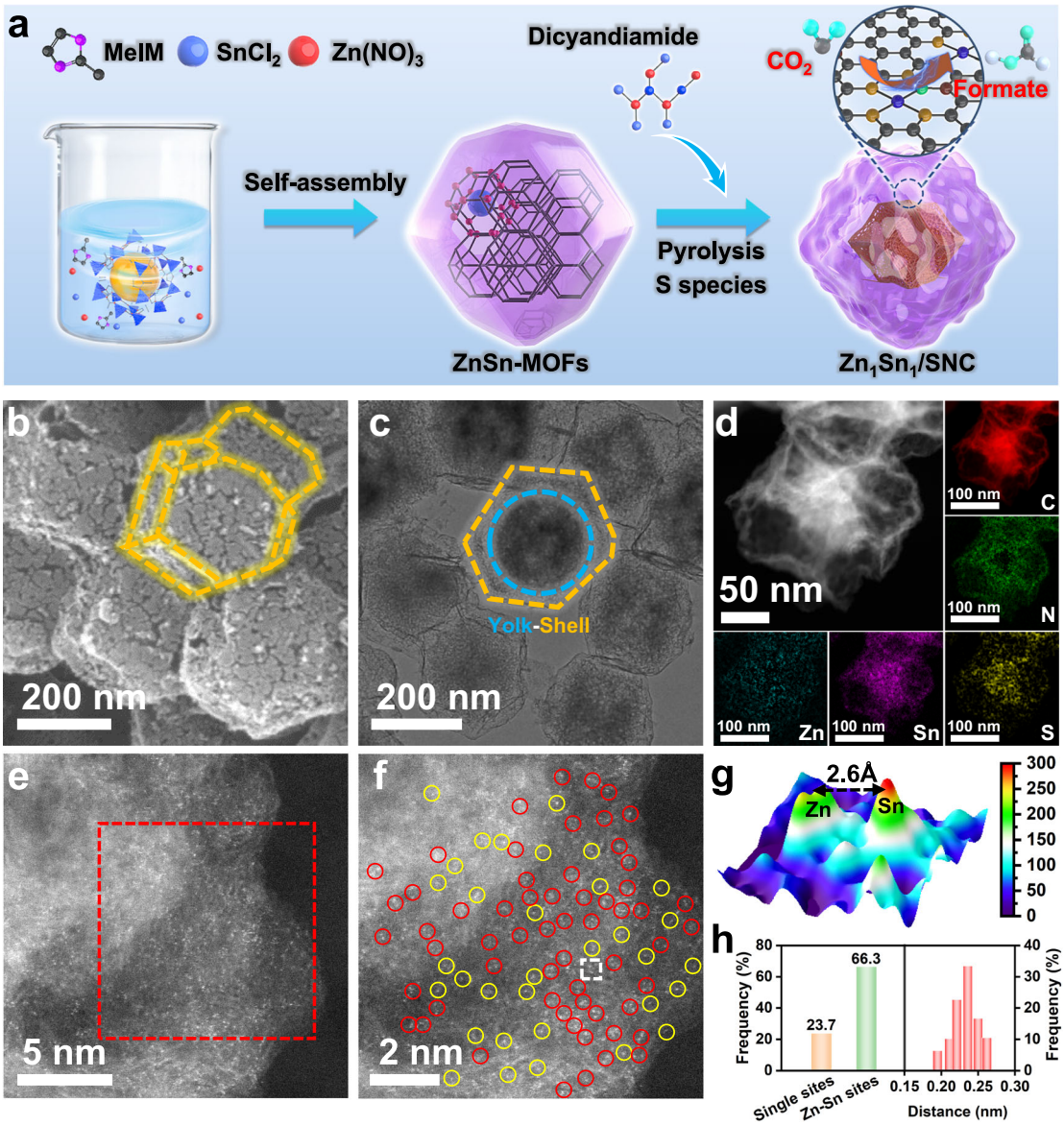

Fig. 1 | Synthesis and structural characterizations of Zn_1Sn_1/SNC DASs. **a** Composite diagram of Zn_1Sn_1/SNC DASs. **b** SEM of Zn_1Sn_1/SNC DASs. **c** TEM of Zn_1Sn_1/SNC DASs. **d** EDS mapping of Zn_1Sn_1/SNC DASs. **e**, **f** AC-STEM image of Zn_1Sn_1/SNC DASs. **g** 3D image simulation of Zn-Sn DASs. **h** Statistical density of the Zn-Sn sites and Zn/Sn single sites, as well as Zn-Sn diatomic distance in the AC-STEM image shown in (**f**). Source data are provided as a Source Data file.

three distinct peaks denoted as a, b, and c, which are associated with the nitrogen present in pyridine and pyrrole assigned to the π* transition, as well as the nitrogen in graphitic structures assigned to the σ* transition.

X-ray absorption fine structure spectroscopy (XAFS) was used to explore the local coordination structure and electronic valence information of the Zn-Sn dual-atom sites (Supplementary Note. 3). X-ray absorption near-edge structure (XANES) was used to determine the chemical valence states of the elements in the samples[51]. The Sn K-edge XANES spectrum (Fig. 2c) shows that the near-edge position of the Sn element in Zn_1Sn_1/SNC is between the energy levels of Sn foil and SnO_2, indicating an oxidation state of Sn in Zn_1Sn_1/SNC ranging from Sn^0 and Sn^{4+}. Furthermore, Fig. 2d demonstrates that the adsorption edge energy position at Zn K-edge falls within the range of values observed for Zn foil and ZnO. The oxidation state of Zn in Zn_1/NC is greater than that in Zn_1Sn_1/SNC, while the oxidation states of tin in Sn_1/NC and Sn_1/SNC are also higher than that in Zn_1Sn_1/SNC. These results indicate that the valence modulation of neighboring metal and coordinating atoms at the Zn-Sn site leads to changes in the oxidation states. In Zn_1Sn_1/SNC, the introduction of S atoms in the partial partition site results in increased electron transfer from the metal center to the S element.

Extended X-ray absorption fine structure (EXAFS) provides information on the polarity, bond length, and bond angle of chemical bonds in materials, which aids the study of their properties and variations. Figure 2e displays the EXAFS spectra of all samples at the Sn K-edge. The results indicate that Zn_1Sn_1/SNC reveals a main signal at 1.42 Å, corresponding to the Sn-N path. Additionally, a shoulder signal at 1.84 Å is observed, distributed among the Sn-S bond scattering peaks. The peak at 2.25 Å is attributed to the Sn-Zn coordination peak signal. In comparison, Sn_1/SNC exhibits two characteristic peaks at 1.44 Å and 1.85 Å, respectively ascribed to the Sn-N and Sn-S coordination signals, suggesting the presence of partial S coordination in Sn_1/SNC, consistent with Sn-S_xN_y characteristics. In contrast, Sn_1/NC only presents a characteristic peak at 1.48 Å, which belongs to the Sn-N signal, indicating exclusive Sn-N coordination in Sn_1/NC. Notably, none of the samples exhibit distinct Sn-Sn feature peaks compared to the Sn foil signal, revealing the dispersed nature of Sn atoms. Similarly, EXAFS spectra (Fig. 2f) reveal the predominant Zn-N (1.52 Å) and Zn-Sn

https://doi.org/10.1038/s41467-025-57573-4

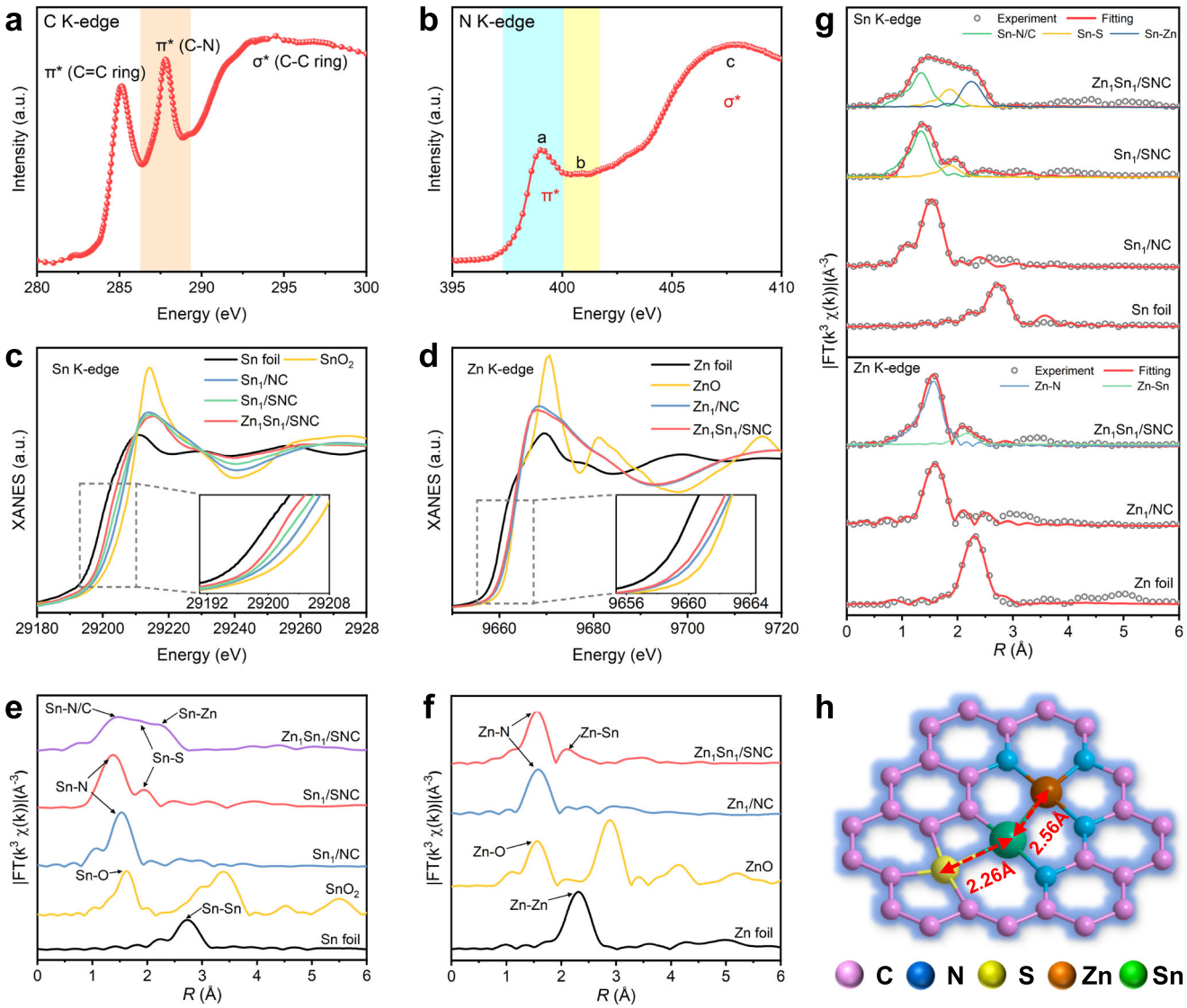

Fig. 2 | Chemical state and local coordination environment of Zn_1Sn_1/SNC DASs. **a** C and (**b**) N K-edge XANES curves. XANES spectra of the Zn_1Sn_1/SNC DASs and the reference samples at (**c**) Sn and (**d**) Zn K-edge. EXAFS spectra of the Zn_1Sn_1/SNC and the reference samples at the (**e**) Sn and (**f**) Zn K-edge, respectively. EXAFS fittings of Zn_1Sn_1/SNC DASs at (**g**) Sn and Zn K-edge. **h** Atomic structure model of Zn_1Sn_1/SNC DASs. Source data are provided as a Source Data file.

(2.22 Å) scattering peak signals in Zn_1Sn_1/SNC at Zn K-edge, whereas Zn_1/NC only displays the Zn-N (1.52 Å) scattering path. These results demonstrate the significant coordination effect among the Zn/Sn dual center and S/N atoms within the first shell, possibly arising from orbital hybridization between the two metals, thereby modulating the oxidation state and coordination environment. Quantitative fitting of the EXAFS spectra (Fig. 2g and S11–18 and Tables S2–S3) allows determination of the coordination parameters for Zn_1Sn_1/SNC and the reference samples, providing specific coordination structures.

Furthermore, the fitting results confirm the presence of partial Zn-Sn bimetallic sites in Zn_1Sn_1/SNC, with Sn metal coordinating both S and N, while Zn coordinates with N. The coordination structures of Sn_1/SNC and Sn_1/NC also align with the expected structures. In conclusion, in Zn_1Sn_1/SNC, direct bonding of bimetallic atoms occurs, and the asymmetric DASs geometric structure, where a single Sn center coordinates one S atom and two N/C atoms, is confirmed as the most likely actual structural configuration, as shown in Fig. 2h.

Electrocatalytic CO_2RR performance of Zn_1Sn_1/SNC

Variations in the metallic sites of Zn_1Sn_1/SNC, Sn_1/SNC, Sn_1/NC, and Zn_1/NC led to differences in CO_2RR activity, measured in a home-made H type cell filled with $KHCO_3$ electrolyte (Supplementary Fig. 19 and Note 4). The incorporation of Zn-Sn bimetallic sites in the yolk-shell structured MOF framework offers a suitable model to investigate CO_2RR performance comprehensively and understand the impact of orbital hybridization. LSV curve from Fig. 3a illustrates the competitive onset voltage of 54 mV for Zn_1Sn_1/SNC. The prominent trend in current density of Zn_1Sn_1/SNC suggests an improved intrinsic CO_2 electroreduction activity. Conversely, the Zn_1/NC sample, lacking Sn doping, demonstrates the lowest CO_2RR activity (Supplementary Fig. 20 and Note 4). Furthermore, the cooperative effect between Zn-Sn metal sites enhances catalytic activity for CO_2 reduction. Performance variations noticed in $KHCO_3$ solutions saturated with Ar and CO_2 indicate the superior catalytic capability of bimetallic sites in converting CO_2 to formate (Supplementary Fig. 21). Figure 3b illustrates the formate Faradaic efficiency of all samples, indicating Zn_1Sn_1/SNC has the highest efficiency. The $FE_{formate}$ value of Zn_1Sn_1/SNC at −0.84 V is 94.6%, notably higher than other catalysts Sn_1/SNC (84.2%), Sn_1/NC (61.2%), and Zn_1/NC (0%). This result highlights the essential function of Sn integration in improving the overall formate product efficiency. We aimed to systematically investigate how different Zn:Sn ratios affect catalytic performance, preparing samples with ratios of 2:1, 1:1,

https://doi.org/10.1038/s41467-025-57573-4

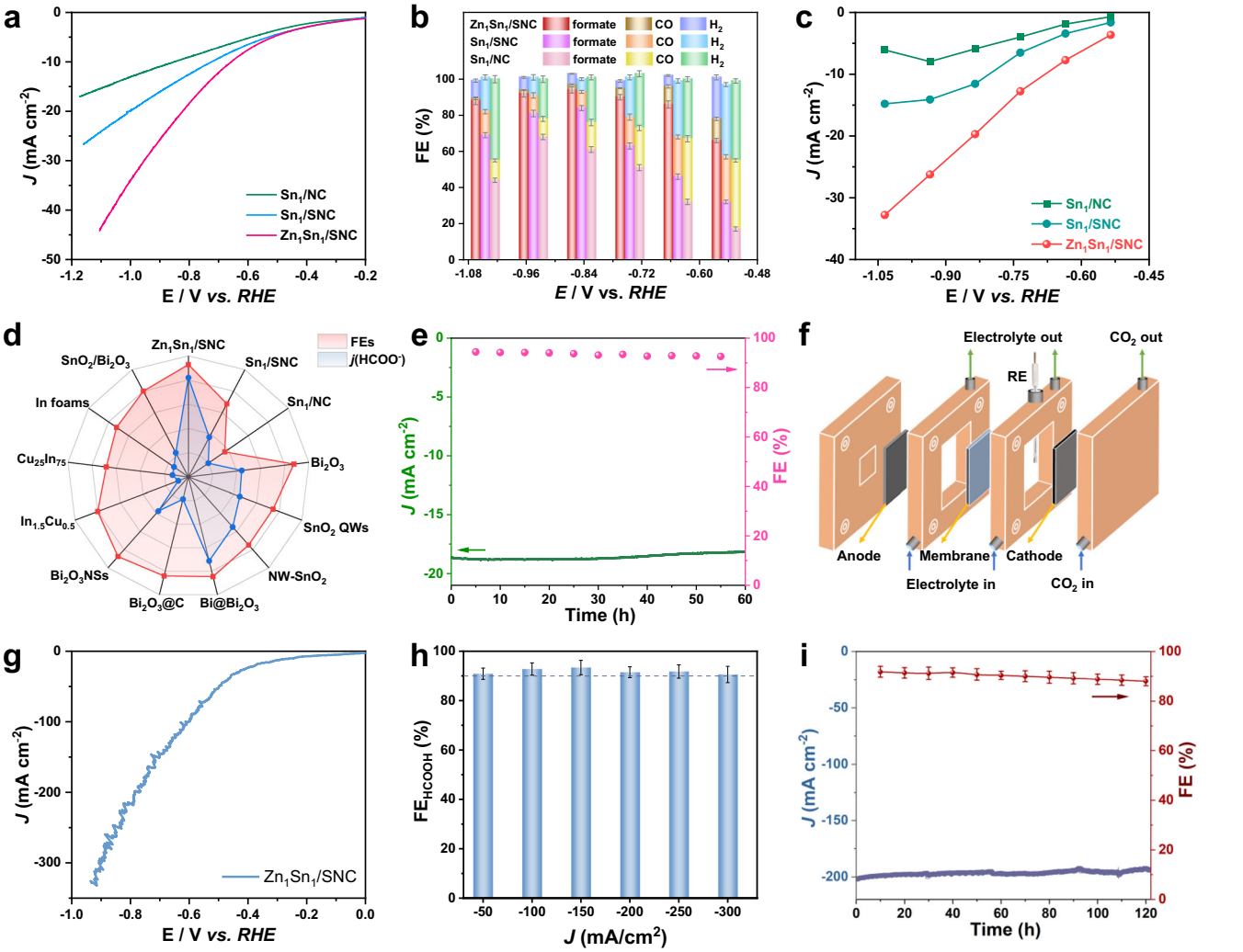

Fig. 3 | Electrochemical CO_2RR properties of Zn_1Sn_1/SNC DASs. a LSV results of Zn_1Sn_1/SNC DASs and the reference samples. The potential was corrected with 90% *iR* compensation. **b** $FE_{formate}$ of Zn_1Sn_1/SNC DASs and the reference samples. All the error bars in (**b**) represent the standard error of the mean. **c** $J_{formate}$ of Zn_1Sn_1/SNC, Sn_1/SNC, Sn_1/NC and Zn_1/NC catalysts. **d** The comparation of FEs for Zn_1Sn_1/SNC DASs with other reported catalysts. **e** Durability test of Zn_1Sn_1/SNC DASs at −0.80 V. **f** Schematic model of flow-cell. **g** LSV curves and (**h**) $FE_{formate}$ of Zn_1Sn_1/SNC DASs. **i** Durability test of Zn_1Sn_1/SNC DASs at −0.75 V. Source data are provided as a Source Data file.

and 1:2. Both higher and lower Zn:Sn ratios impact catalyst performance, so the final ratio was set at 1:1 (Supplementary Fig. 23). To identify potential liquid phase products, ^{1}H nuclear magnetic resonance spectroscopy (NMR) analysis was performed, revealing the presence of signals corresponding to formate product (Supplementary Fig. 22). Figure 3c clearly shows the partial current densities of the formate products ($J_{formate}$) of the individual samples, indicating that Zn_1Sn_1/SNC has the highest current density at all reaction potentials. The $J_{formate}$ of Zn_1Sn_1/SNC achieves 32.8 mA/cm^2 at −1.04 V, which is significantly higher than the Zn_1/NC (−14.8 mA/cm^2), and Sn_1/NC (−6.08 mA/cm^2), and the $J_{formate}$ of Zn_1Sn_1/SNC raises rapidly with increased potentials. With this regard, Zn_1Sn_1/SNC demonstrates superior selectivity for formic acid and higher current density than previously reported catalysts and control samples (Fig. 3d and Table S4). The distinctive asymmetric structure of Zn_1Sn_1/SNC enables it to retain stability after continuous catalysis for 60 h, with the $FE_{formate}$ above 94% (Fig. 3e). The morphology and structure of the sample after durability testing exhibit minimal changes. Characterization results show that the yolk-shell structure is preserved, with zinc and tin maintaining their dispersed atomic properties (Figs. S24–26). During the entire reaction process, there is minimal metal leaching, leading to negligible variations in metal content pre- and post-reaction (Table S1). Overall, the durability of Zn_1Sn_1/SNC is significantly enhanced by its asymmetric structure and the inherent stability of the MOF.

Subsequently, additional assessment of the overall CO_2RR performance of Zn_1Sn_1/SNC under industrial current conditions was conducted utilizing a custom-designed flow-cell structure (Fig. 3f and S27). The LSV curve data suggests that enhancements to the gas diffusion electrode result in increased current density in the CO_2RR process, reaching −315.2 mA cm^{-2} at −0.90 V. Moreover, a high level of formate selectivity is ensured at increased currents, exceeding 90.6% across a wide range of current densities from 50 to 300 mA cm^{-2}, as illustrated in Fig. 3h. The Zn_1Sn_1/SNC material demonstrates favorable stability for a duration of 120 h when subjected to a potential of -0.75 V, while maintaining a steady operation current. (Fig. 3i). Throughout the entire 120-h stability test, the $FE_{formate}$ measurements maintained around 89.7% per hour. Calculated from the single carbon yield equation, the single carbon yields of Zn_1Sn_1/SNC, Sn_1/SNC and Zn_1/SNC at -0.84 V were 9.8%, 5.7% and 2.9%, respectively (Supplementary Fig. 28). The Zn_1Sn_1/SNC has the highest single carbon yield, implying a fuller and more efficient utilization of CO_2 in Zn_1Sn_1/SNC.

https://doi.org/10.1038/s41467-025-57573-4

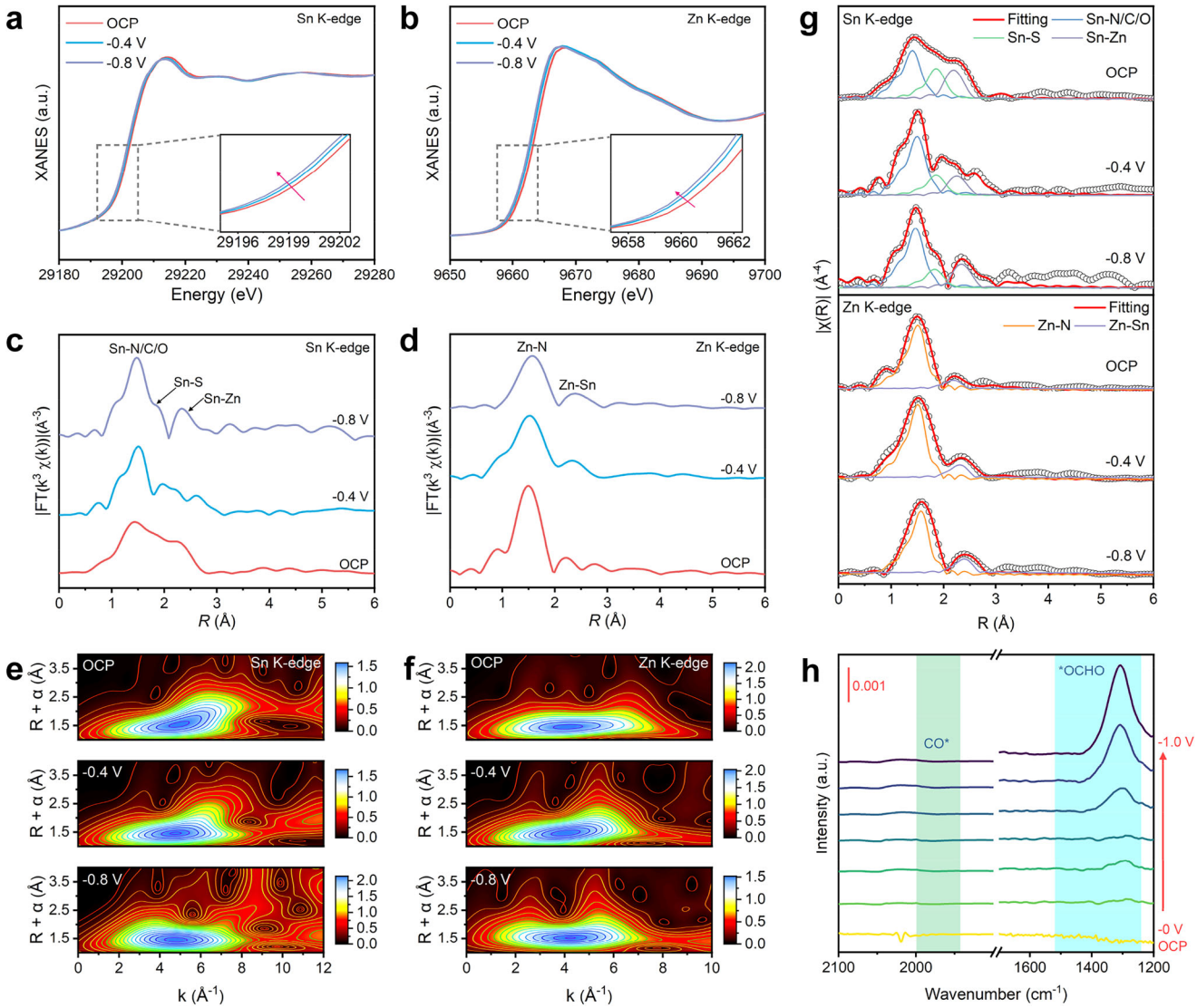

Fig. 4 | In situ XAFS characterization of Zn_1Sn_1/SNC DASs. a Sn and (**b**) Zn K-edge XANES spectra of the Zn_1Sn_1/SNC at different applied potentials. The illustration is a magnification of the absorbed edge. FT-EXAFS of Zn_1Sn_1/SNC with and without applying voltage at (**c**) Sn and (**d**) Zn K-edge. WT-EXAFS plots of Zn_1Sn_1/SNC at different potentials at (**e**) Sn and (**f**) Zn K-edge. **g** FT-EXAFS fitting curve of Zn_1Sn_1/SNC with and without applying voltage at Zn and Sn K-edge. **h** In situ ATR-FTIR test on Zn_1Sn_1/SNC. Source data are provided as a Source Data file.

Mechanism study of asymmetric Zn-Sn dual atom sites for boosting CO_2 to formate

To elucidate the dynamic structural characteristics of the Zn-Sn DASs, the in-situ experimental measurements were conducted during real-working conditions[52,53] (Supplementary Fig. 29 and Note. 5-6). In Fig. 4a, the XANES spectra show a negative energy shift of the Sn absorption edge as the system transitions from the open circuit potential (OCP) state to −0.40 V to −0.80 V, covering a range of approximately 2.3 eV. These migrations display a reduction in the oxidation states observed at the Sn site. In contrast to the standard Sn foil and SnO, the oxidation state of Sn within the Zn-Sn DASs consistently falls within an intermediate range, as revealed in the first-derivative spectra (Supplementary Fig. 30). These results show that the Sn oxidation states of OCP, −0.4 V and −0.8 V are 1.036, 0.727 and 0.596, respectively. Likewise, the absorption threshold of Zn exhibits a downward shift in energy during reaction conditions (Fig. 4b) The oxidation states of Zn at OCP, -0.4 V and -0.8 V are 0.962, 0.833 and 0.740, respectively, indicating that the valence states also decrease with the gradual decrease of voltage (Supplementary Fig. 31). Such occurrences are ascribed to the creation of Sn−O linkages resulting from the interplay between Zn-Sn dual-site and absorbed CO_2, consequently instigating the reorganization of electrons within Zn, Sn, N, S, and O in CO_2. This electronic rearrangement may lead to hybridization of d-p electronic orbitals between the two Zn-Sn metals. The active sites of Sn and Zn experience a reduction in their valence states under in-situ measurements, with both valence states falling within the range of 0 to 2+. Besides, the EXAFS spectra (Fig. 4c, d) show the asymmetric Zn-Sn dual site as it undergoes twisting and stretching within a permissible range as a result of its interaction with CO_2, while maintaining a stable local configuration during CO_2RR. The changes of WT-EXAFS at different potentials are also clearly shown that the increase in potential causes some contraction of the Zn-Sn bond (Fig. 4e, f). The results indicate that the coordination of the Zn-Sn sites undergoes some changes during the reaction, which leads to a better formate selectivity of the newly formed stable coordination structure. The specific EXAFS fittings were derived from the data presented in Fig. 4g and S32–33, and are documented in Table S5, S6. The absorption edge at the Zn and Sn K-edges demonstrates an elevation under OCP conditions in contrast to the original XANES spectra. This rise is believed to be attributed to the CO_2 adsorption mechanism (CO_2(g) + *

https://doi.org/10.1038/s41467-025-57573-4

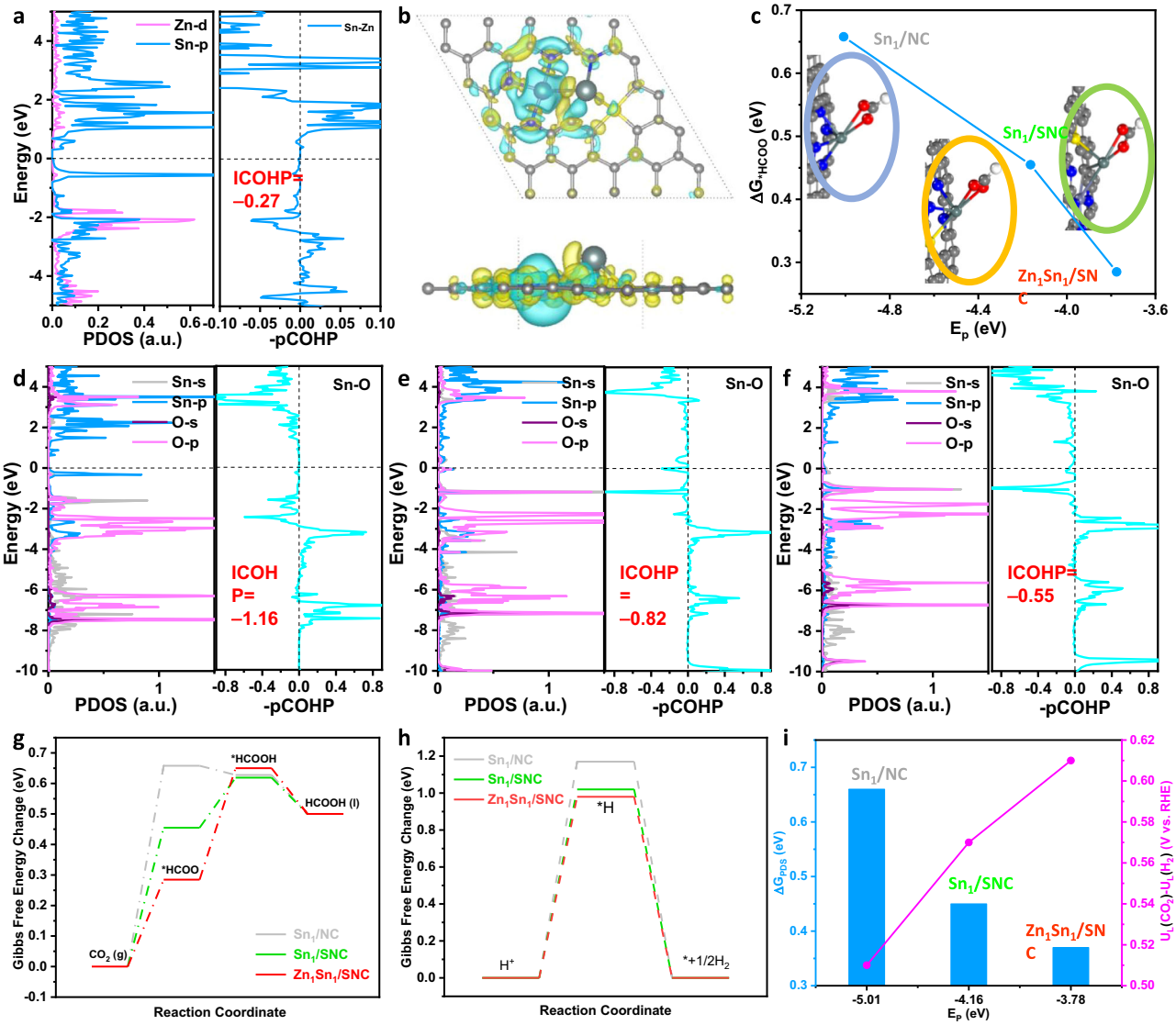

Fig. 5 | Theoretical CO_2RR activity of Zn_1Sn_1/SNC DACs. a Partial density of states and COHP data of Zn d orbitals and Sn p orbitals. **b** Differential charge density between Zn atom and residual atom in the Zn_1Sn_1/SNC DACs, the yellow and cyan contour with the surface value of 0.002 e/bohr^3 marks augmented and reduced charge density, respectively. **c** The relationship between the adsorption energy of HCOO and p band center of Sn atom. Inset is the adsorption configuration of HCOO intermediate. **d**–**f** pCOHP analysis of Sn atom and O atom of *HCOO species on the Sn_1/NC, Sn_1/SNC, and Zn_1Sn_1/SNC. The horizontal red line marks the fermi level. **g**, **h** he free energy change of CO_2 reduction to HCOOH and HER. **i** Comparison of ΔG_{PDS} and $U_L(CO_2)$-$U_L(H_2)$ (V vs. RHE) on the Sn_1/NC, Sn_1/SNC, and Zn_1Sn_1/SNC. Source data are provided as a Source Data file.

+ $e^- \leftrightarrow {}^*CO_2^-$). As a negative potential is introduced, there is a downward shift in the absorption edge energy, leading to a reduction in the valence state of Zn and Sn. This suggests a swift conversion of CO_2 and the elimination of adsorbed formate molecules at Zn-Sn dual sites.

In order to further correlate the catalytic pathway at the Zn-Sn active site, in-situ attenuated total reflectance Fourier transform infrared spectroscopy (ATR-FTIR) was performed to detect the key intermediates in CO_2RR[54] (Supplementary Note. 7). The ATR-FTIR spectra, which are dependent on the applied potentials, were acquired by incrementally decreasing the potentials from 0 to −1.0 V, as illustrated in Fig. 4h. In an electrolyte solution containing 0.1 M $KHCO_3$ saturated with CO_2, the infrared spectrum recorded at OCP state is regarded as the baseline reference, with no distinctive group signals initially observed. In the process of CO_2RR, it is suggested that the conversion of CO_2 to formate (*OCHO) is more effective than the conversion to *COOH. In experimental tests conducted on Zn_1Sn_1/SNC catalyst, a distinct peak corresponding to *OCHO at approximately 1308 cm^{-1} was observed, and this peak exhibited an increasing intensity as the applied potentials decreased. Additionally, CO* characteristic peaks typically appeared around 1950 cm^{-1}. The results showed that Zn_1Sn_1/SNC did not adsorb significant CO* intermediates during the reaction, indicating that CO was not the major product.

Density functional theory (DFT) method investigated the effect of *p-d* orbital coupling over asymmetrical Zn-Sn motif on the HCOOH yield in the Zn_1Sn_1/SNC model, compared with Sn_1/NC and Sn_1/SNC models in Supplementary Fig. 34, Supplementary data 1, and Note. 8[55]. Supplementary Fig. 35 and S36 displayed the ab-initio molecule dynamics (AIMD) simulation results with 300 K and 700 K conditions, indicating the thermodynamical stability of Zn_1Sn_1/SNC configuration. To reveal the influence of *p-d* orbital hybridization on the active Sn site, the partial density of states (PDOS) and crystal orbital overlap population (COHP) results of Zn and Sn atom for the Zn_1Sn_1/SNC model were calculated in Fig. 5a and S37. Under the fermi level of 5 eV, the PDOS intensity of Zn and Sn atom was mainly attributed by *3d* and *5p* orbitals, respectively, which all possessed large orbital overlaps with negative integrated COHP (ICOHP) value of −0.27. Differential charge

density result of Zn_1Sn_1/SNC structure between Zn atom and remanent atoms indicated evident charge transfer from Zn atom to Sn atom, simultaneously reinforcing Sn-S binding strength, as shown in Fig. 5b. Specifically, Supplementary Fig. 38 displayed the PDOS and COHP results of Sn and coordinated S/N atom for the said models. In the energy range from −10 to 0 eV, the *5 s* and *5p* orbitals of Sn atom and *3p* orbitals of S atom or *2p* orbitals of N atom also owned wide energy superpositions with ICOHP value of −1.60 for Zn_1Sn_1/SNC, −1.39 for Sn_1/SNC, and −1.33 for Sn_1/NC. Noting that the more negative value marks stronger binding strength. It meant that *p-d* orbital coupling over Zn-Sn atom pair can significantly enhance the Sn-S binding strength, benefiting for maintaining the charge states of active Sn site. Considering the feature of Lewis acid for CO_2 molecule, the charge reservoir of active sites was ulteriorly calculated within the scheme of Bader charge analysis to investigate the disparity of HCOOH yield. In the Sn_1/NC surface, the Sn atom reduced 1.25 electrons to coordinated N-C system. Following the implanting of less electronegativity S or Zn atom to break the symmetry of active center, the transferred electron numbers of Sn atom gradually decreased to 1.16 for Sn_1/SNC and 0.98 for Zn_1Sn_1/SNC, demonstrating powerful electron reservoir capacity of Sn atoms with the *p-d* orbital coupling over asymmetrical Sn-Zn dual-atom. Interestingly, the charged number of active Sn atom (1.25, 1.16, and 0.98 e^-) was negatively proportional to the p-band center position (E_p) of p-block element (−5.01, −4.16, and −3.78 eV) in Supplementary Fig. 39, which was termed as an effective activity descriptor resembling with traditional d-band center (E_d).

To verify the relationship between the adsorption intensity of key intermediates and E_p of active Sn atom for CO_2 reduction to HCOOH product, the adsorption of HCOO species was simulated on the Sn_1/NC, Sn_1/SNC and Zn_1Sn_1/SNC surface. Their adsorption energies of HCOO intermediate (ΔG_{*HCOO}) were 0.66, 0.45, and 0.28 eV, respectively, which was also negatively correlated to E_p value of Sn site, corresponding adsorption configurations were displayed in Fig. 5c. Noting that the less positive adsorption energy value signifies strong binding strength. The higher energy level of E_p close to the fermi level led to stronger uptake of HCOO species, specifically for Zn_1Sn_1/SNC configuration. Figure 5d–f showcased the PDOS and COHP results of Sn atom and bonding O atom of HCOO. In the energy range from −10 to −3 eV, the *5s* and *5p* orbitals of Sn atom and *2p* orbitals of O atom have wide orbital coupling, which all dedicated to the bonding states of Sn-O bond in the said models. From −3 eV to fermi level, the above orbitals hybridizations mainly contributed to the antibonding states of Sn-O bond. The higher energy level position and intensity of antibonding states generates the weaker binding strength for Sn_1/NC and Sn_1/SNC, indicating strongest Sn-O bond for the adsorption of HCOO on the Zn_1Sn_1/SNC model. It has a positive correlation between the adsorption energies of HCOO species and ICOHP value for the said models, such as, −1.16 for Zn_1Sn_1/SNC, −0.82 for Sn_1/SNC, and −0.55 for Sn_1/NC, as shown in Supplementary Fig. 40.

In the CO_2 2e^- reduction to HCOOH process, the adsorption of key intermediate COOH or H for competitive reaction to CO or H_2 was also calculated on the abovementioned models. Supplementary Figs. 41–S43 marked the optimized adsorption configurations and adsorption energies. The adsorption energies of COOH and H were also negatively proportional to the E_p value, same as that of HCOO species. It substantiated adequately that E_p can be served as an effective activity descriptor. Their adsorption energies of HCOO were distinctly lower than that of COOH and H, demonstrating preferential generation of HCOO in the electrochemical CO_2 reduction process. Figure 5g showcased the free energy change of CO_2 2e^- reduction to HCOOH, the potential-determined step (PDS) on the Sn_1/NC model was the first protonation step to HCOO species with the free energy change of 0.66 eV, then reduced to be 0.45 eV on the Sn_1/SNC model. Zn_1Sn_1/SNC ulteriorly decreased the hydrogenation barrier of first step with 0.28 eV, but enhanced the next protonation barrier to HCOOH with 0.37 eV, which served as the PDS of the generation of HCOOH from CO_2 molecule, also lower than that of Sn_1/NC and Sn_1/SNC models. Compared with the COOH pathway to CO in Supplementary Fig. 44, the adsorption energies of HCOO on the said models were all lower than that of COOH, such as Sn_1/NC (1.86 eV), Sn_1/SNC (1.66 eV), and Zn_1Sn_1/SNC (1.29 eV), benefiting to produce HCOOH rather than CO product. Figure 5h displayed their free energy changes of HER, e.g., Sn_1/NC (1.17 eV), Sn_1/SNC (1.02 eV), and Zn_1Sn_1/SNC (0.98 eV), the uptake of H on the active Sn site is the PDS, their free energy changes were significantly higher than that of HCOOH product. Previous studies proposed that the disparity of limited potential for CO_2 reduction and HER [$U_L(CO_2)$-$U_L(H_2)$] reflected the selectivity of CO_2 reduction where a more positive $U_L(CO_2)$-$U_L(H_2)$ value demonstrated higher selectivity[56–58]. Figure 5i depicted the relationship between ΔG_{PDS}/$U_L(CO_2)$-$U_L(H_2)$ and E_p value for CO_2 reduction to HCOOH, indicating Zn_1Sn_1/SNC possessed best activity and selectivity because of its least ΔG_{PDS} (0.37 eV) and largest $U_L(CO_2)$-$U_L(H_2)$ value (0.61 V). Above all, the activity and selectivity of CO_2 reduction to HCOOH product was ulteriorly boosted on the Zn_1Sn_1/SNC model, which was correlated with the *p* band energy level position of active Sn atom induced by the *p-d* orbital coupling with the construction of asymmetrical Zn-Sn bond.

Discussion

In conclusion, an asymmetric Zn-Sn DASs, where metal centers coordinate with different main group heteroatoms (S or N), is successfully synthesized using a ligand coetching method, demonstrating good CO_2RR performance. Enhanced metal site adsorption capability is achieved through distinct hybridization of *d-p* orbitals, contributing to high catalytic process selectivity. The Zn_1Sn_1/SNC exhibits a notable increase in the faradaic efficiency for formate production in both H-cell and flow-cell. DFT calculations and multispectral in situ characterization results further confirm that the asymmetric Zn-Sn site effectively enhances *HCOO species adsorption strength in CO2RR, indicating catalytic behavior on Zn-Sn DASs. Our findings not only create insights into the *d-p* orbital hybridization in CO_2RR, but also offer new perspectives for gaining a deeper understanding of the unique electronic effects of asymmetric sites and their mechanisms of structure-activity.

Methods

Chemicals

Zinc nitrate hexahydrate ($Zn(NO_3)_2{\cdot}6H_2O$), Tin chloride ($SnCl_2$), Potassium bicarbonate ($KHCO_3$, 99.999%), Nafion D-521 dispersion (5% wt in water and 1-propanol), 2-methylimidazole, sulfur powder were purchased from Alfa Aesar. Dicyandiamide, methanol and ethanol were obtained from Sinopharm Chemical. Nafion 211/117 membrane was purchased from Dupont. 18.2 MΩ/cm ultrapure water was pured by milli-Q instrument. High purity Helium gas (99.9999%) and carbon dioxide (99.999%) were purchased from Haipu Gas Company. All the chemicals and gases were analytical grade and used without further purification.

Preparation of Zn_1Sn_1/SNC and Sn_1/SNC samples

Typically, 2.94 g $Zn(NO_3)_2{\cdot}6H_2O$ and 120 mg $SnCl_2$ were added synchronously into 80 ml of methanol solution for stirring 30 min. Then, 3.24 g 2-methylimidazole was dissolved in 80 ml methanol solution. The metal precursor solution was added immediately into the above ligand solution and stirred constantly for 5 h. The powders (ZnSn-MOFs) were obtained by washing with methanol for several times and drying at 60 °C in a vacuum oven for overnight. And the ZnSn-MOFs was prepared by a ligand coetching approach. Firstly, the sulfur ground with dicyandiamide powder (upstream) and ZnSn-MOFs powder (downstream) were placed successively in a tubular furnace, and then pyrolysis at 1000 °C with a rate of 5 °C min^{-1} under an Ar atmosphere for 2 h. The as-obtained Zn_1Sn_1-SNC catalyst was directly

used for electrochemical and characterization tests without further treatment. The Sn_1-SNC catalyst was prepared by similar procedures except for using 0.5 M H_2SO_4 to etch the Zn species. Zn_2Sn_1/SNC and Zn_1Sn_2/SNC were prepared by the same procedure, only the precursor ratio of Zn and Sn needed to be adjusted to 2:1 and 1: 2.

Preparation of Zn_1/NC and Sn_1/NC samples

Typically, 2.94 g $Zn(NO_3)_2{\cdot}6H_2O$ and 120 mg $SnCl_2$ were added synchronously into 80 ml of methanol solution for stirring 30 min. Then, 3.24 g 2-methylimidazole was dissolved in 80 ml methanol solution. The metal precursor solution was added immediately into the above ligand solution and stirred constantly for 5 h. The powders (ZnSn-MOFs) were obtained by washing with methanol for several times and drying at 60 °C in a vacuum oven for overnight. The Zn_1-NC catalyst was prepared by direct pyrolysis of ZIF-8 at 1000 °C with a rate of 5 °C min^{-1} under an Ar atmosphere for 4 h.

Preparation of Zn_1/NC and Sn_1/NC samples

Typically, 2.94 g $Zn(NO_3)_2{\cdot}6H_2O$ and 120 mg $SnCl_2$ were added synchronously into 80 ml of methanol solution for stirring 30 min. Then, 3.24 g 2-methylimidazole was dissolved in 80 ml methanol solution. The metal precursor solution was added immediately into the above ligand solution and stirred constantly for 5 h. The powders (ZnSn-MOFs) were obtained by washing with methanol for several times and drying at 60 °C in a vacuum oven for overnight. The Sn_1/NC catalyst was prepared by first pyrolysis of ZIF-8 at high temperature, then the residual Zn species were removed by acid etching, and then the Sn species was impregnated. Under the protection of Ar atmosphere, the pyrolysis was conducted at 1000 with a rate of 5 °C min^{-1} for 2 h.

Electrochemical measurements for CO_2RR

The CO_2RR experiments were executed on a CHI 760e electrochemical workstation with a H-type cell filled with 0.1 M $KHCO_3$ electrolyte. Pt foil and Ag/AgCl (saturated KCl) were used as the counter electrode and reference electrode, respectively. Nafion 211 membrane was separated the cathodic chamber and anodic before adding 0.1 M $KHCO_3$ solution. Before the formal measurement, the $KHCO_3$ solution was pured by bubbling Ar for 30 min and then switched to CO_2. The LSV curves were conducted at scan rate of 10 mV/s with persistent bubbling CO_2 at flow rate of 15 sccm via an accurate mass flowmeter. All the potential was reported versus the reversible hydrogen electrode (RHE) and corrected by iR-drop compensation. The potential was corrected with 90% *iR* compensation. The gas products were checked via the Shimazu 2010 plus gas chromatography (GC), which was equipped with BID detector and ShinCarbon ST 100/120 packed column. High purity helium (99.9999%) was used as the carrier gas for the GC. The liquid products were checked by the ^1H NMR spectra through a Bruker AV 400 MHz NMR spectrometer, which uses D_2O and DMSO as solvent and internal standard (^1H NMR: D_2O at 4.69 ppm, DMSO at 2.71 ppm).

Flow-cell device measurement details

The fresh Zn_1Sn_1-SNC sample was sprayed on GDL (28 BC, Sinero Store) with a loading of 1 mg cm^{-2} as the working electrode (cathode). RuO_2 (Sinero Store) sprayed on GDL (28 BC, Sinero Store) with a loading of 1 mg cm^{-2} was used as the counter electrode (anode). A proton exchange membrane (Nafion 117) was inserted between the cathodic chamber and anodic chamber of the flow cell. On cathode side, electrolyte (0.5 M $KHCO_3$) was pumped by a syringe pump with a constant flow rate of 15 sccm. High purity CO_2 gas was flowed at a rate of 30 sccm behind the cathode GDL. An Ag/AgCl (saturated KCl) reference electrode was employed. The solution resistance was determined by potentiostatic electrochemical impedance spectroscopy at frequencies ranging from 0.1 Hz to 100 kHz. All the measured potentials using three-electrode setup were manually compensated.

Data availability

The data supporting the findings of this study are available within the article and its Supplementary Information files. All other relevant source data are available from the corresponding authors. Source data are provided with this paper.

References

1. Schoedel, A., Ji, Z. & Yaghi, O. M. The role of metal–organic frameworks in a carbon neutral energy cycle. *Nat. Energy* **1**, 16034 (2016).
2. Zhong, M. et al. Accelerated discovery of CO_2 electrocatalysts using active machine learning. *Nature* **581**, 178–183 (2020).
3. Guo, X. et al. Grid integration feasibility and investment planning of offshore wind power under carbon-neutral transition in China. *Nat. Commun.* **14**, 2447 (2023).
4. Tian, Q. et al. Mesoporous carbon spheres with programmable interiors as efficient nanoreactors for H_2O_2 electrosynthesis. *Nat. Commun.* **15**, 983 (2024).
5. Deng, G. et al. Body-Centered-Cubic-Kernelled $Ag_{15}Cu_6$ Nanocluster with Alkynyl Protection: Synthesis, Total Structure, and CO_2 Electroreduction. *J. Am. Chem. Soc.* **145**, 3401–3407 (2023).
6. Lees, E. W. et al. Gas diffusion electrodes and membranes for CO_2 reduction electrolysers. *Nat. Rev. Mater.* **7**, 55–64 (2022).
7. Liu, W. et al. Isolated Cu-Sn diatomic sites for enhanced electroreduction of CO_2 to CO. *Nano Res.* **16**, 8729–8736 (2023).
8. Zhang, P. et al. Surface Ru–H bipyridine complexes-grafted TiO_2 nanohybrids for efficient photocatalytic CO_2 methanation. *J. Am. Chem. Soc.* **145**, 5769–5777 (2023).
9. Sun, Z. et al. Sulfur-bridged asymmetric cuni bimetallic atom sites for CO_2 reduction with high efficiency. *Adv. Mater.* **36**, e2404665 (2024).
10. Su, J. et al. Recent development of nanomaterials for carbon dioxide electroreduction. *SmartMat* **3**, 35–53 (2022).
11. Fang, W. et al. Durable CO_2 conversion in the proton-exchange membrane system. *Nature* **626**, 86–91 (2024).
12. Xie, Y. et al. High carbon utilization in CO_2 reduction to multi-carbon products in acidic media. *Nat. Catal.* **5**, 564–570 (2022).
13. Guo, W. et al. Asymmetric Cu sites for enhanced CO_2 electroreduction to C_{2+} products. *CCS Chem.* **0**, 1–9 (2023).
14. Chu, A. T. et al. Organic non-nucleophilic electrolyte resists carbonation during selective CO_2 electroreduction. *J. Am. Chem. Soc.* **145**, 9617–9623 (2023).
15. Zhang, J. et al. Tuning the reaction path of CO_2 electroreduction reaction on indium single-atom catalyst: Insights into the active sites. *Nano Res* **15**, 4014–4022 (2022).
16. Xu, Q.-J. et al. Understanding oxygen vacant hollow structure CeO_2@In_2O_3 heterojunction to promote CO_2 reduction. *Rare Met* **42**, 1888–1898 (2023).
17. Wang, Q. et al. Recent advances in copper-based catalysts for electrocatalytic CO_2 reduction toward multi-carbon products. *Nano Res. Energy* **3**, e9120112 (2024).
18. Deng, Y. et al. Operando spectroscopic analysis of axial oxygen-coordinated single-Sn-atom sites for electrochemical CO_2 reduction. *J. Am. Chem. Soc.* **145**, 7242–7251 (2023).
19. Chang, B. et al. Electrochemical reduction of carbon dioxide to multicarbon (C_2+) products: challenges and perspectives. *Energy Environ. Sci.* **16**, 4714–4758 (2023).
20. Dong, J. et al. Continuous electroproduction of formate via CO_2 reduction on local symmetry-broken single-atom catalysts. *Nat. Commun.* **14**, 6849 (2023).
21. Han, N. et al. Ultrathin bismuth nanosheets from in situ topotactic transformation for selective electrocatalytic CO_2 reduction to formate. *Nat. Commun.* **9**, 1320 (2018).
22. Bi, J. et al. High-rate CO2 electrolysis to formic acid over a wide potential window: An electrocatalyst comprised of indium

nanoparticles on chitosan-derived graphene. *Angew. Chem., Int. Ed.* **62**, e202307612 (2023).
23. Wang, N. et al. Suppressing the liquid product crossover in electrochemical CO_2 reduction. *SmartMat* **2**, 12–16 (2021).
24. Cho, J. et al. 2D Metal/Graphene and 2D metal/graphene/metal systems for electrocatalytic conversion of CO_2 to formic acid. *Angew. Chem. Int. Ed*. **63**, e202320268 (2024).
25. Wang, T. et al. Halogen-incorporated Sn catalysts for selective electrochemical CO_2 Reduction to Formate. *Angew. Chem., Int. Ed.* **62**, e202211174 (2023).
26. Ruan, S. et al. Bismuth nanosheets with rich grain boundaries for efficient electroreduction of CO_2 to formate under high pressures. *Chin. J. Catal.* **43**, 3161–3169 (2022).
27. Jiang, X. et al. Boosting CO_2 electroreduction to formate via bismuth oxide clusters. *Nano Res.* **16**, 12050–12057 (2023).
28. Li, S. et al. Ampere-level CO_2 electroreduction with single-pass conversion exceeding 85% in acid over silver penetration electrodes. *Nat. Commun.* **15**, 6101 (2024).
29. Bok, J. et al. Designing atomically dispersed Au on tensile-strained Pd for efficient CO_2 electroreduction to formate. *J. Am. Chem. Soc.* **143**, 5386–5395 (2021).
30. Wang, J.-J. et al. A review of non-noble metal-based electrocatalysts for CO_2 electroreduction. *Rare Met* **40**, 3019–3037 (2021).
31. Shen, J. & Wang, D. How to select heterogeneous CO_2 reduction electrocatalyst. *Nano Res. Energy* **3**, e9120096 (2024).
32. Ding, J. et al. A tin-based tandem electrocatalyst for CO_2 reduction to ethanol with 80% selectivity. *Nat. Energy* **8**, 1386–1394 (2023).
33. Li, L. et al. Copper as a single metal atom based photo-, electro-, and photoelectrochemical catalyst decorated on carbon nitride surface for efficient CO_2 reduction: A review. *Nano Res. Energy* **1**, 9120015 (2022).
34. Kim, J. et al. A red-light-powered silicon nanowire biophotochemical diode for simultaneous CO_2 reduction and glycerol valorization. *Nat. Catal*. **7**, 977–986 (2024).
35. Lian, Z., Dattila, F. & López, N. Stability and lifetime of diffusion-trapped oxygen in oxide-derived copper CO_2 reduction electrocatalysts. *Nat. Catal.* **7**, 401–411 (2024).
36. Sun, Z. & Chen, W. Proximity effect of binuclear catalyst for plastics recycling. *Matter* **6**, 2562–2564 (2023).
37. Li, Y. et al. Synergistic effect of atomically dispersed Ni–Zn pair sites for enhanced CO_2 electroreduction. *Adv. Mater.* **33**, 2102212 (2021).
38. Chai, Y. et al. Dual-atom catalyst with N-colligated Zn1Co1 species as dominant active sites for propane dehydrogenation. *J. Am. Chem. Soc.* **146**, 263–273 (2024).
39. Zhang, L. et al. Hybrid double atom catalysts for hydrogen evolution reaction: A sweet marriage of metal and nonmetal. *Adv. Energy Mater*. **14**, 2302754 (2024).
40. Wang, L. et al. Axial dual atomic sites confined by layer stacking for electroreduction of CO_2 to tunable syngas. *J. Am. Chem. Soc.* **145**, 13462–13468 (2023).
41. Mo, S. et al. Non-interacting Ni and Fe dual-atom pair sites in N-doped carbon catalysts for efficient concentrating solar-driven photothermal CO_2 reduction. *Angew. Chem., Int. Ed.* **62**, e202313868 (2023).
42. Zhang, Z.-J. et al. Modulating *p-d* orbital hybridization by CuO/Cu nanoparticles enables carbon nanofibers high cycling stability as anode for sodium storage. *Rare Met* **42**, 4039–4047 (2023).
43. Sun, T. et al. Strengthened d-p orbital-hybridization of single atoms with sulfur species induced bidirectional catalysis for lithium–sulfur batteries. *Adv. Funct. Mater.* **33**, 2306049 (2023).
44. Liu, G. et al. Strengthened d–p orbital hybridization through asymmetric coordination engineering of single-atom catalysts for durable lithium–sulfur batteries. *Nano Lett.* **22**, 6366–6374 (2022).
45. Han, Z. et al. Engineering d-p orbital hybridization in single-atom metal-embedded three-dimensional electrodes for Li–S batteries. *Adv. Mater.* **33**, 2105947 (2021).
46. Shang, H. et al. Engineering unsymmetrically coordinated Cu-S_1N_3 single atom sites with enhanced oxygen reduction activity. *Nat. Commun.* **11**, 3049 (2020).
47. Pei, J. et al. Integrating host design and tailored electronic effects of Yolk–Shell Zn–Mn diatomic sites for efficient CO_2 electroreduction. *Angew. Chem., Int. Ed.* **63**, e202316123 (2024).
48. Pei, J. et al. A replacement strategy for regulating local environment of single-atom Co-S_xN_{4-x} catalysts to facilitate CO_2 electroreduction. *Nat. Commun.* **15**, 416 (2024).
49. Zu, X. et al. Efficient and robust carbon dioxide electroreduction enabled by atomically dispersed $Sn^{\delta+}$ sites. *Adv. Mater.* **31**, 1808135 (2019).
50. Chen, P. et al. Interfacial engineering of cobalt sulfide/graphene hybrids for highly efficient ammonia electrosynthesis. *PNAS* **116**, 6635–6640 (2019).
51. Zhang, J. et al. Tuning the coordination environment in single-atom catalysts to achieve highly efficient oxygen reduction reactions. *J. Am. Chem. Soc.* **141**, 20118–20126 (2019).
52. Su, X. et al. Complementary Operando Spectroscopy identification of in-situ generated metastable charge-asymmetry Cu_2-CuN_3 clusters for CO_2 reduction to ethanol. *Nat. Commun.* **13**, 1322 (2022).
53. Yang, Y. et al. Operando studies reveal active Cu nanograins for CO_2 electroreduction. *Nature* **614**, 262–269 (2023).
54. Liu, K. et al. Ultra-fast pulsed discharge preparation of coordinatively unsaturated asymmetric copper single-atom catalysts for CO_2 reduction. *Adv. Funct. Mater*. **34**, 202312589 (2024).
55. Pei, W. et al. Investigation of dual atom doped single-layer MoS2 for electrochemical reduction of carbon dioxide by first-principle calculations and machine-learning. *J. Mater. Inf.* **3**, 26 (2023).
56. Wang, L. et al. Axial dual atomic sites confned by layer stacking for electroreduction of CO_2 to tunable syngas. *J. Am. Chem. Soc.* **145**, 13462–13468 (2023).
57. Li, X. et al. Exclusive Ni-N_4 sites realize near-unity CO selectivity for electrochemical CO_2 reduction. *J. Am. Chem. Soc.* **139**, 14889–14892 (2017).
58. Ren, W. et al. Isolated diatomic Ni-Fe metal-nitrogen sites for synergistic electroreduction of CO_2. *Angew. Chem. Int. Ed.* **58**, 6972–6976 (2019).

Acknowledgements

This work was supported by the National Natural Science Foundation of China (22375019). This work was supported by Guangxi Minzu University Scientific Research Fund Funding Project (Introduction of Talents Scientific Research Start-up Project under Grant No.2020KJQD18), Guangxi Natural Science Foundation (2023GXNSFBA026279), Guangxi Science and Technology Base and Special Funding for Talents (Guike AD21220068). This work was supported by the Start-up Foundation for Senior Talents of Jiangsu University (21JDG041), and the China Postdoctoral Science Foundation (2023M731357). We thank the theoretical calculations performed on the Northwest District of the Sugon National Supercomputer Center and the A6 Zone of the Beijing Super Cloud Computing Center, supported by PARATERA. The authors thank the BL1W1B in the Beijing Synchrotron Radiation Facility (BSRF), BL14W1 in the Shanghai Synchrotron Radiation Facility (SSRF), BL12B in the National Synchrotron Radiation Laboratory (NSRL) for help with characterizations.

Author contributions

W. C. conceived the idea, designed the study and wrote the paper. B. P. and H.S. performed most of the reactions, collected and

analyzed the data, and wrote the paper. B. P. performed electron-microscopy characterizations. Z.W., Z.S. (Zhiyi Sun) and Z.D. carried out the X-ray absorption fine structure characterizations. B.P., H.S., Z.S. (Zhiyi Sun) and W.C. conducted the electrochemical measurements. Z.S. (Zhongti Sun) performed the DFT calculations. H.S., Z.W., Z.S. (Zhongti Sun) and W.C. helped to check and revise the paper. Z.S. (Zhongti Sun) and Z.D. performed some of the experiments and revised the paper.

Competing interests

The authors declare no competing interests.

Additional information

Supplementary information The online version contains supplementary material available at https://doi.org/10.1038/s41467-025-57573-4.

Correspondence and requests for materials should be addressed to Wenxing Chen.

Peer review information *Nature Communications* thanks Fa Yang, Yujin Ji, and the other, anonymous, reviewer(s) for their contribution to the peer review of this work. A peer review file is available.

Reprints and permissions information is available at http://www.nature.com/reprints

Publisher's note Springer Nature remains neutral with regard to jurisdictional claims in published maps and institutional affiliations.

Open Access This article is licensed under a Creative Commons Attribution-NonCommercial-NoDerivatives 4.0 International License, which permits any non-commercial use, sharing, distribution and reproduction in any medium or format, as long as you give appropriate credit to the original author(s) and the source, provide a link to the Creative Commons licence, and indicate if you modified the licensed material. You do not have permission under this licence to share adapted material derived from this article or parts of it. The images or other third party material in this article are included in the article's Creative Commons licence, unless indicated otherwise in a credit line to the material. If material is not included in the article's Creative Commons licence and your intended use is not permitted by statutory regulation or exceeds the permitted use, you will need to obtain permission directly from the copyright holder. To view a copy of this licence, visit http://creativecommons.org/licenses/by-nc-nd/4.0/.

© The Author(s) 2025